IEEE Access
Multidisciplinary ⋮ Rapid Review ⋮ Open Access Journal

Received January 26, 2021, accepted February 3, 2021, date of publication February 8, 2021, date of current version February 23, 2021.

Digital Object Identifier 10.1109/ACCESS.2021.3057681

Probabilistic Slider: A Tool for Visualizing Fuzzy Segmentation Uncertainties

JI MA[1], JINJIN CHEN[2], LIYE CHEN[3], JIAZHOU CHEN[1], XUJIA QIN[1], AND MINGYU BAO[1]

[1]School of Computer Science and Technology, Zhejiang University of Technology, Hangzhou 310023, China
[2]School of Design and Art, Communication University of Zhejiang, Hangzhou 310018, China
[3]Sir Run Run Shaw Hospital, School of Medicine, Zhejiang University, Hangzhou 310058, China

Corresponding authors: Ji Ma (maji@zjut.edu.cn) and Jinjin Chen (chenjinj@cuz.edu.cn)

This work was supported in part by the National Natural Science Foundation of China under Grant 61902350, in part by the Open Project Program of the State Key Lab of CAD&CG of Zhejiang University under Grant A2111, in part by the Cultural Relic Protection Science Foundation of Zhejiang Province under Grant 2020014, and in part by the Natural Science Foundation of Zhejiang province under Grant LY20F020025.

ABSTRACT Visualization of classification uncertainty of the medical materials is very significant, as different classifications may lead to different visualization results, and different results may cause completely different diagnosis or pre-operative planning decisions, and thus have different consequences to patients. Traditional Direct Volume Rendering (DVR) enables medical experts to visualize the classification uncertainty by random adjustment of the transfer function. However, three main problems exist by using this method: first, the resulting renderings do not indicate any quantitative information about the classification uncertainty of different materials; second, the resulting renderings are randomly revealed by random adjustment of the TF; third, both classification task and optical property assignment task are mixed together in one step. These problems may make this method (1) fail to enable medical experts to make accurate diagnosis or pre-operative planning decision; (2) unable to provide medical experts with a clear concept of how medical volume data are classified. To address these problems, we proposed a probabilistic slider system, which compared to the traditional DVR, enables medical experts to make more accurate diagnosis or pre-operative planning decision, and have a clearer concept of how the medical volume data being classified.

INDEX TERMS Medical visualization, material classification, uncertainty, direct volume rendering, decision support.

I. INTRODUCTION

In medical visualization, classification is a very important but complex task, and uncertainty exists in classification, which for the same dataset, may lead medical experts to make completely different diagnosis or pre-operative planning decisions, and thus may have significantly different consequences to a patient. On the other hand, DVR has been accepted as a routine tool in clinical work, which enables medical experts to visualize the classification uncertainty by random adjustment of Transfer Function (TF). However, using DVR to visualize classification uncertainty has three main problems: (1) its results could not indicate any quantitative information. This could mislead medical experts to assume that the observed result is the true case, although it may be not because of classification uncertainty, and thus make inappropriate or even wrong diagnosis or pre-operative planning base on the result. Also, for multiple results, they cannot inform the user which one would more likely happen; (2) its results are revealed randomly because of random adjustment of the TF. This could result in some results that play important roles in diagnosis or pre-operative planning may be lost, and thus lead medical experts to make inappropriate or even wrong diagnosis or pre-operative planning. Also, for arbitrary one material, this may be impossible to reveal its two extreme cases (maximum and minimum probabilities of occurrence), which can be used as boundary conditions to make a decision; (3) it mixes classification and optical property assignment tasks together, and thus makes medical experts unclear about how medical volume data being classified. To address these problems, we presented a probabilistic slider system, which can be used to visualize classification uncertainty in medical volume data. Compared to traditional DVR, it has the following advantages: (1) it generates results that could

The associate editor coordinating the review of this manuscript and approving it for publication was Jiachen Yang.

quantitatively indicate the probability of occurrence of arbitrary one material; (2) it enables to reveal all possible appearances of arbitrary one material in a quicker and systematic way; (3) it enables to reveal the extreme cases of arbitrary one material, which can be used as boundary conditions to make a decision; (4) it enables more easily removing or adding materials for rendering; (5) it separates the classification task and optical property assignment task that are usually mixed in TF. As a result, it enables medical experts to make more accurate diagnosis or pre-operative planning decision, and have a clearer concept of how the medical volume data being classified.

II. RELATED WORK

Our research falls into the field of uncertainty visualization, which has been identified as one of the main challenges in the visualization community [1]–[3]. Many techniques have been proposed to contribute to this field over the past years. Brodlie *et al.* [4] and Potter *et al.* [5] presented two review works on summarizing and categorizing the state-of-the-art uncertainty visualization techniques. Both works categorize these techniques based on the dimension (0D—3D) and type (scalar, multifield, vector, tensor) of data to be visualized. However, as their categorizing works are based on the characteristics of data rather than the characteristics of techniques, the techniques that are essentially the same technique could be divided for different data. In comparison, Lei *et al.* [6] presented a review work which summarizes and categorizes uncertainty visualization techniques based on their characteristics. Their work divided the state-of-the-art techniques into the following four main categories:

•Glyph. This method first encodes uncertainty to glyphs, and then distributes and displays these glyphs on data. Probably the most classic and simple example of this method is error bar, which uses statistics such as mean, lower bound and upper bound of errors to encode error bars, and then distributes and displays them on the data. Another classic example is box plot [7], which in its most basic form uses five summary statistics including upper bound, lower bound, upper quartile, lower quartile and median to encode box plots, and then distributes and displays them on the data. Other examples include [8]–[15]. The advantages of the glyph method are simple and easy to understand, but its disadvantage is that it could easily cause problems such as visual clutter.

•Visual variable encoding. This method uses various visual variables e.g., positions, shapes, brightness, color, texture, direction, etc. to encode uncertainty. For example, color is one of the most common visual variable, which can encode uncertainty by mapping them to different uncertainties [16]–[21]. Another example is transparency, which can also be used to encode uncertainty by mapping them to different uncertainties [22]–[24]. Other examples include [25]–[29]. The advantage of the visual variable encoding method is that it could enable users to quickly identify the magnitude and region of uncertainty, but its disadvantage is that visual variables need to be selected carefully to effectively express uncertainty.

•Geometry. This method uses the distribution or attributes of generated geometries e.g., points, lines, surfaces, grids, volumes, etc. to encode uncertainty. One example is the spaghetti plot proposed by Potter *et al.* [30], which utilizes the distribution of lines that compose the spaghetti plot to encode the uncertainty of ensemble data. Other examples include [31]–[37]. The advantages of this method is that it is intuitive, easy to understand, and can be used to encode multiple uncertainties by using complex geometries. Its disadvantage is that the generated geometries could easily occlude the visualization results of those certain data.

•Animation. This method uses parameters relevant to animation e.g., speed, range of movement, sequence of movement, etc. to encode uncertainty, and users have to persistently observe the animation to find out the magnitude and region of uncertainty. One classic example is the animated visual vibration technique proposed by Brown [38], which utilizes the amplitude of a curved surface to encode uncertainty. Other examples include [39], [40]. The advantage of animation is that it expresses uncertainty in a more vivid way. Its disadvantage are that: compared to those static uncertainty visualization techniques, it needs longer time for users to understand; also, it could cause visual fatigue because of the movement and flickering in animation.

While a number of works have been proposed as mentioned above, little works have been focused on uncertainty visualization in medical data that include a large amount of uncertainty, ranging from medical imaging step over several data processing steps, to the final rendering step. This is extremely significant for medical experts to make more accurate diagnostic decision. Lundstrom *et al.* [39], [40] presented a work that utilizes the display speed of animation to enable medical experts to visualize the classification uncertainty in medical volume data. However, a disadvantage of their method is that it could cause visual fatigue. In contrast to their method, our method will not cause this problem. Recently, Ristovski *et al.* [41] presented a work that identify what types of uncertainty exist in medical visualization and what their characteristics are in terms of mathematical models. Such a work provides us a solid foundation to explore uncertainty visualization techniques in medical data so as to enable medical experts to make more accurate diagnosis.

There also have been many theories developed and proposed for measuring the uncertainty, such as the extended fuzzy sets, evidence theory, D numbers theory and information quality. However, as our research focuses on uncertainty visualization, they are out of the scope of our research.

III. PROBABILISTIC SLIDER

The workflow of Probabilistic Slider can be summarized in Fig. 1. It is clear that this workflow consists of in total of four steps, which are intensity transformations, Spatial Fuzzy C-means (SFCM) classification, material optical property specification and query-based color encoding, and volume

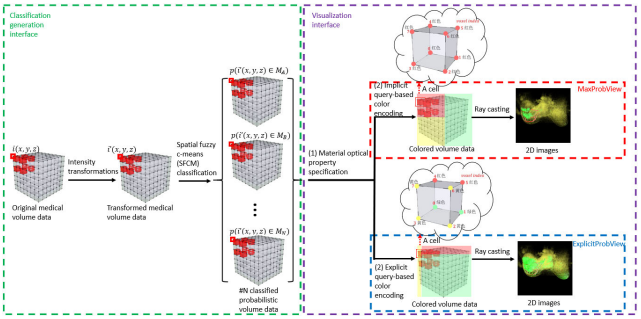

FIGURE 1. The workflow of probabilistic slider.

rendering, respectively. The following four subsections introduce each of these steps in detail.

A. INTENSITY TRANSFORMATIONS

Given the original medical volume data in which there is an intensity value $i(x, y, z)$ associated with each voxel (x, y, z), the first step of our workflow is to apply intensity transformations to it to obtain the transformed medical volume data. As a result, for each voxel (x, y, z) in the transformed medical volume data, it has a transformed intensity value $i'(x, y, z)$. The reason of applying intensity transformations is simple but not trivial: they could not only enhance the contrast of medical data, but also allow users to filter out those uninterested volume data while reserving the interested volume data. This will benefit our workflow's second step, which aims to produce a good classification result [42]. Thus, the intensity transformations can be considered as a pre-processing operation prior to classification. Fig. 2 demonstrates the effects of intensity transformations for Bruce and CT Neck datasets, respectively. In particular, Fig. 2(a)-2(c) demonstrate how the intensity transformations are able to enhance the contrast among different medical materials, while Fig. 2(d)-2(f) show how they allow users to filter out uninterested materials such as skin and soft tissues (note how these materials are removed from the dataset) while keeping the interested materials such as thyroid tumor and carotid arteries.

In this research, three intensity transformation methods have been applied to transform the original medical volume data, as listed below:

•The Sigmoid function. This is also referred to as Logistic function, which can be modeled as Equation (1):

$$\mathrm{i}' = \mathrm{c}\frac{1}{1+\mathrm{e}^{-\frac{\mathrm{i}-\omega}{\sigma}}} \tag{1}$$

where i represents the intensity values of original medical volume data; i' represents the transformed intensity values; c is a constant, and it refers to a range into which the transformed intensity values could fall; both ω and σ are two user-adjustable parameters of this function, and they represent the center and width of the intensity value distribution of original medical volume data, respectively.

•Automated Contrast Optimization. For users with less experience of intensity transformations, we provide them with the Automated Contrast Optimization method, to help them quickly and automatically enhance their data's contrast. This method has two variations. The first variation is to form a new maximum and minimum boundary of data by removing an identical user-specified percentage of total voxels from both sides of histogram. The second variation is to from a new maximum and minimum boundary of data by removing one user-specified percentage of total voxels from the left side of histogram, and removing another user-specified percentage of total voxels from the right side of histogram.

•Interactive Intensity TF. To provide users with greater flexibility of intensity transformations, a more general intensity TF interface has been designed, where users can form any TFs by moving, adding or deleting their nodes. In addition, the histogram of original medical volume data is displayed as background of this interface to guide users to form their TFs.

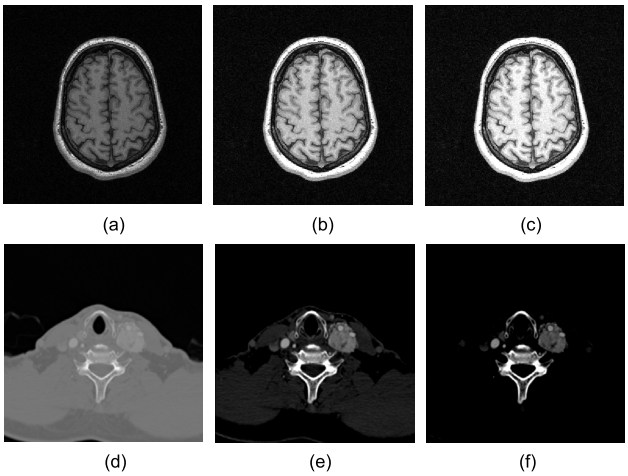

FIGURE 2. The effects of intensity transformations. In particular, (a)-(c) show how the intensity transformations can enhance the contrast among different medical materials for the Bruce dataset, and (d)-(f) show how they allow users to filter out uninterested materials and only reserve the interested materials for the CT Neck dataset.

B. SPATIAL FUZZY C-MEANS CLASSIFICATION

Given the transformed medical volume data obtained from the intensity transformations, the second step of the workflow is to apply the SFCM classification method on them so as to obtain N classified probabilistic volume data. Here N represents the number of classifications determined by users, and it usually depends on the number of materials incorporated in the transformed medical volume data e.g., if there are five materials incorporated in the transformed medical volume data, then N could be 5; however, users could specify an arbitrary number for N rather than 5, and in those cases, materials to be classified are either merged or subdivided. During the classification, each voxel's intensity value $i'(x, y, z)$ in the transformed medical volume data is transformed to N probability values $p\left(i'(x, y, z) \in M_A\right), \ldots, p(i'(x, y, z) \in M_N)$, which represent the possibilities that this voxel's intensity value belongs to each of these materials $M_A, \ldots, M_N$.

For the classification, we use the SFCM clustering method proposed by Chuang *et al.* [43] and extends it for volume data. This method can be summarized as follows:

(1) Assign an initial guess value for each cluster center c_i;

(2) Given each cluster center c_i from step (1), update the probability value p_{ij} (also known as membership value) of each voxel's intensity value v_j belonging to each cluster c_i, by using Equation (2):

$$\mathrm{p_{ij}} = \frac{1}{\sum_{\mathrm{k=1}}^{\mathrm{N}} \left(\frac{\|\mathrm{v_j - c_i}\|}{\|\mathrm{v_j - c_k}\|}\right)^{2/(\mathrm{m-1})}} \tag{2}$$

where N represents the number of clusters (one cluster corresponds to one classification); m is a constant parameter and it controls the fuzziness of the resulting classification; $m = 2$ is used in this work; $\|\|$ refers to the norm.

(3) Given the probability value p_{ij} from step (2), calculate the spatial function for each voxel's intensity value v_j in each cluster c_i, by using Equation (3):

$$\mathrm{h_{ij}} = \sum\nolimits_{\mathrm{k}\in \mathrm{NB(v_j)}} \mathrm{p_{ik}} \tag{3}$$

where $NB(v_j)$ represents a cube window centered on the voxel with intensity value being v_j (*NB* refers to the word "neighbor"). In this work, a $5 \times 5 \times 5$ window is used to calculate the spatial function h_{ij}.

(4) Given the probability value p_{ij} from step (2) and the spatial function h_{ij} from step (3), re-calculate the probability value p'_{ij} (which is the final probability value at each iteration) of each voxel's intensity value v_j belonging to each cluster c_i, by using Equation (4):

$$\mathrm{p_{ij}^{'}} = \frac{\mathrm{p_{ij}^{p} h_{ij}^{q}}}{\sum_{\mathrm{k=1}}^{\mathrm{N}} \mathrm{p_{kj}^{p} h_{kj}^{q}}} \tag{4}$$

where p and q are constant parameters to control the relative importance of both functions. In Chuang *et al.*'s work [43], they point out that when $p = q = 1$, SFCM shows the best clustering results. Thus $p = q = 1$ is used in this work.

(5) Given the re-calculated probability value p'_{ij} from step (4), update each cluster center c_i, by using Equation (5):

$$\mathrm{c_i^{'}} = \frac{\sum_{\mathrm{j=1}}^{\#\text{of voxels}} \mathrm{p_{ij}^{'m} v_j}}{\sum_{\mathrm{j=1}}^{\#\text{of voxels}} \mathrm{p_{ij}^{'m}}} \tag{5}$$

(6) If $\|c'_i - c_i\| < \varepsilon$ (here ε refers to the convergence criterion, which is a constant), then stop iteration; otherwise $c_i = c'_i$, and proceed to the next iteration from step (2) to step (6).

Fig. 3 shows the classification effects of SFCM for the Breast Tumor dataset under different N. More specifically, in Fig. 3(a), $N = 4$, and in Fig. 3(b), $N = 5$. Note how the breast tumor as illustrated in Fig. 3(a) is classified as more refined materials as shown in Fig. 3(b).

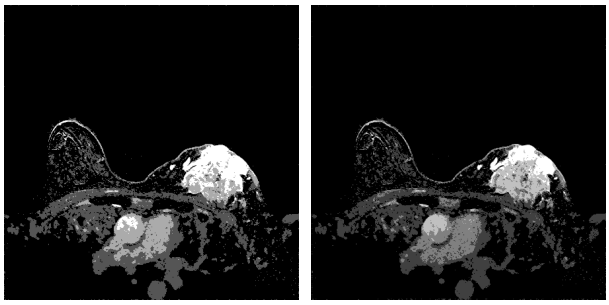

FIGURE 3. The classification effects of SFCM for the Breast Tumor dataset under different number of classifications. In (a), $N = 4$, and in (b), $N = 5$.

C. MATERIAL OPTICAL PROPERTY SPECIFICATION AND QUERY-BASED COLOR ENCODING

Given N classified probabilistic volume data, the workflow's third step consists of two sub-steps: (1) users specify optical property $RGB\alpha$ for each material classified as one cluster so as to generate the optical property Look-up Table (LUT), (2) a query needs to be formed, so that based on the query we can color each voxel. As a result, the colored volume data are generated, with each voxel being assigned with an appropriate color.

For the material optical property specification sub-step, users could choose any optical property but not gray for a material, because gray is reserved for use to indicate those voxels whose maximum probability concurrently belong to more than one material. The advantages of allowing users themselves to customize each material's property optical is obvious: it is easier for them to interpret the query feedback by examining the optical properties in the final images.

For the query-based color encoding sub-step, there are two types of query to be formed: implicit query and explicit query. Each type of query has its own color encoding method, as introduced below.

1) IMPLICIT QUERY-BASED COLOR ENCODING

An implicit query is automatically formed by our system, and the color encoding based on the query is as follows: for each voxel, we try to find out to which material it most likely belongs to (by comparing its N probability values), and we assign its color with that material's color. In this way, we could present users a MaxProbView, which shows a most possible result of the data to be visualized. One case here deserves special mentioning: sometimes it is possible that some voxels most likely belong to more than one material, and in that case, the above-mentioned way of assigning color to a voxel is useless. As a solution to this problem, we assign gray with *50%* transparency to those voxels, so that when gray areas appeared on the final images, they indicate that the voxels included in these areas most likely belong to more than one material.

2) EXPLICIT QUERY-BASED COLOR ENCODING

An explicit query can be formed by users through dragging the material sliders when holding down the left button of

mouse, as shown in Fig. 5. The color encoding based on the query for each voxel is as follows: (1) if this voxel's probability of belonging to the currently queried material match the query, then it is colored as the color of the currently queried material; (2) otherwise we will find out to which material it most likely belongs to. If it most likely belongs to only one material but not the currently queried material, then it is colored as that material's color; if it most likely belongs to more than one material, then it is colored as the gray with *50%* transparency. Here one case deserves special mentioning: it is possible that this voxel's probability of belonging to the currently queried material does not match the query, and thus it cannot be colored as the color of the currently queried material; however, it may most likely belong to the currently queried material, and thus should have been colored as the color of currently queried material. This is a conflict, and it could result in that when the currently queried material's color appeared on the final images, users cannot determine whether it matches the query, or it most likely belongs to the currently queried material. To resolve the conflict so that the currently queried material's color appeared on the final images only indicates match of the query, we assign transparent for this voxel. As a result of explicit query-based color encoding, we could present users another ExplicitProbView, which combines a query-match result for the currently queried material, and a most possible result for other materials.

D. VOLUME RENDERING

Given the colored volume data generated from the previous step, the final step is to apply ray casting rendering on them to obtain 2D resulting images. One thing deserves special mentioning here: instead of using trilinear interpolation, the nearest neighbor interpolation is used to obtain each sample's optical property. This is because trilinear interpolation may introduce non-user-specified optical properties to the final images, which could prevent users from interpreting the results. However, the nearest neighbor interpolation will not cause such an issue.

IV. IMPLEMENTATION

The system has been completely implemented, which consists of two separate sub-systems. The first sub-system is an interface used for generating classification (as illustrated by the left big box in Fig. 1), and it implements the first two steps mentioned in the workflow. The second sub-system is a visualization interface (as illustrated by the right big box in Fig. 1), which takes the classification result generated from the first sub-system as input, and finally display the visualization results. It implements the last two steps of the workflow. The following two subsections introduce the two sub-systems, respectively.

A. CLASSIFICATION GENERATION INTERFACE

Fig. 4 shows a Matlab implementation of the classification generation interface, which consists of four modules,

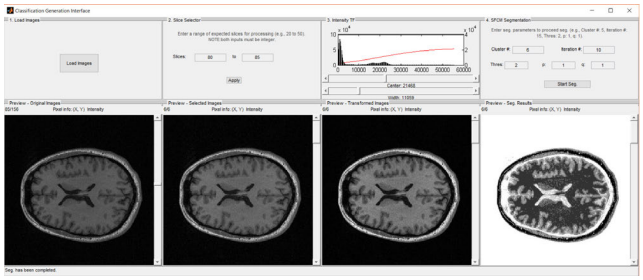

FIGURE 4. An overview of classification generation interface.

as shown from left to right, with each module having both function part and its corresponding preview part. The first module is loading images module, where users could load an original medical volume data expected to explore, and the ''Preview – Original Images'' window displays the corresponding results slice by slice. The second module is slice selector module, where users could specify a subset of the loaded original medical volume data to explore, in case they are only interested in features on a subset. But of course, they could reserve the original medical volume data to explore. The ''Preview – Selected Images'' window shows the corresponding results slice by slice. The third one is intensity transformation module, which can be any of the three methods mentioned in Section III.A (Fig. 4 only shows the Sigmoid method out of the three methods) and is specified by users. Users adjust the parameters associated with their specified method in this module, and the ''Preview – Transformed Images'' window shows the corresponding results slice by slice after intensity transformation. The fourth one is SFCM classification module, where users need to specify five parameters of the SFCM method mentioned in Section III.B for classification. After convergence of this method, a defuzzification process is applied, where each voxel is assigned to a specific cluster to which it most likely belongs, and the ''Preview – Seg. Results'' window shows the corresponding classification results slice by slice. Here the iteration number parameter deserves special mentioning, it is used as an optional convergence criterion in addition to the threshold parameter, and enables users to terminate the classification if the number of iterations in classification has been reached.

The classification generation interface sub-system is designed so that users can repeatedly refine parameters to obtain a satisfied classification result. For each module's preview part, users could use scrollbar to navigate through different slices and position mouse cursor on a specific pixel at a slice to inspect its intensity values. Finally, this sub-system produces a text file, which lists names of the N classified probabilistic volume data to be loaded into the visualization interface sub-system.

B. VISUALIZATION INTERFACE

Fig. 5 shows a GPU-accelerated QT and CUDA implementation of the visualization interface, which has a very simple layout. To obtain renderings in the MaxProbView and

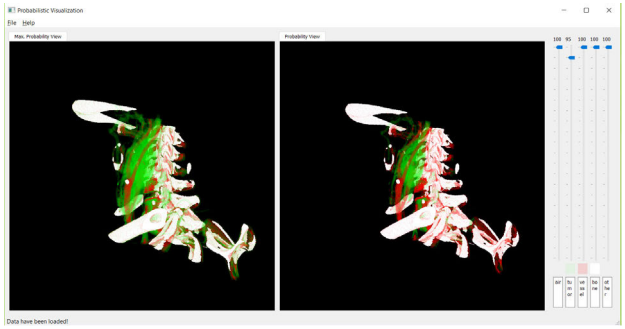

FIGURE 5. An overview of visualization interface. The left view is the MaxProbView, and the right view is the ExplicitProbView.

TABLE 1. The information of datasets used in this research.

Dataset	Dimensions	Bits Per Voxel
Breast Tumor	448×448×208	16
CT Neck	512× 512 × 300	16
Angio	384× 512 × 80	8
Bruce	256× 256 ×81	16

ExplicitProbView, users need to perform the following steps: first, they need to specify an above-mentioned text file to load corresponding data, and this can be done by using the Open option under File menu. Second, as illustrated at the right bottom corner of Fig. 5, for each material (or cluster), users need to specify an optical property for it by clicking its corresponding optical property button. Optionally, they could also type in a name for each material e.g., air, tumor, in case there are too many materials to remember. As a result of these two steps, renderings appear in the MaxProbView. Third, users now could perform explicit queries for certain material by dragging its slider. As a result, renderings corresponding to the queries appear in the ExplicitProbView. Both views are arranged side by side for ease of comparison, and for each view, it can be rotated, translated and zoomed in or out, so that users can easily observe data from all perspectives.

V. RESULTS AND DISCUSSION

To demonstrate the usefulness of the probabilistic slider, we applied it to four datasets and compared it with the traditional DVR. Table 1 summarizes the information of the four datasets used in this research.

In clinical work, accurate assessment of the extent of a breast tumor is a very important task, and different assessment results may have significantly different impacts on a patient. This is because the breast tumor is surrounded by many complex breast tissues, and any damage of these breast tissues may result in serious consequences to the patient. If we have removed the breast tumor with excessive tissues, then the patient may get injured or lose certain functions e.g., feeding. However, if we have removed it incompletely, then it may regrow, and the patient has to repeatedly undergo painful and expensive operations. Fig. 6(a) shows a visualization result of the Breast Tumor dataset by using traditional DVR, which has two problems: (1) it could not indicate any quantitative

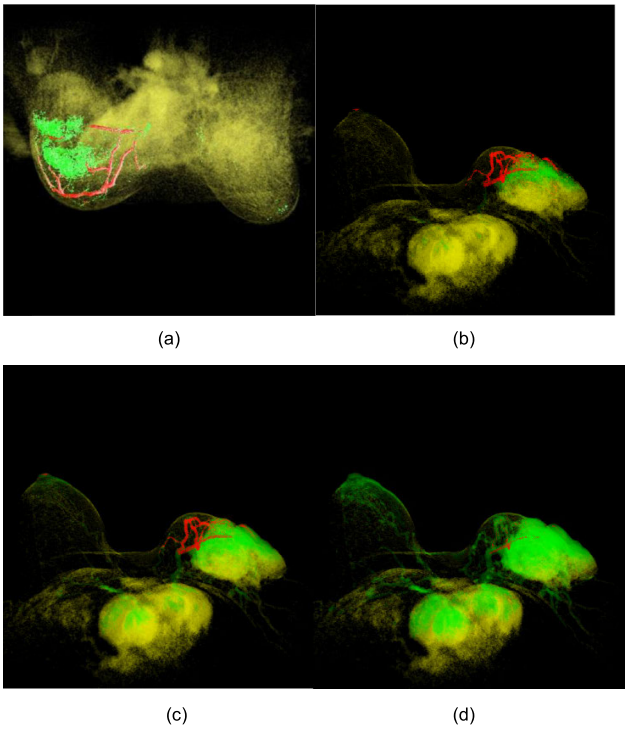

FIGURE 6. (a) shows a rendering of Breast Tumor dataset using traditional DVR. Green represents breast tumor, red represents vessels, and yellow represents other breast materials. (b)-(d) show breast tumor's three probability query results (from left to right, the breast tumor's probabilities are *99%*, *50%* and *1%*, respectively) in our system's ExplicitProbView.

information of how likely the green part is the breast tumor. This tends to mislead medical experts to assume that the green part shown on the result is true case of the breast tumor, although it maybe not because of the classification uncertainty, and thus make inappropriate or even wrong diagnosis or pre-operative planning decision based on this result. For experienced medical experts, they may adjust TF to evaluate other possible results of the breast tumor. However, when they inspect the results, they cannot be informed which one would more likely happen; (2) it is revealed randomly due to random adjustment of the TF. Suppose it is true case of the breast tumor but not revealed because of the random adjustment, then medical experts may never make appropriate or correct diagnosis or pre-operative planning decision. Fig. 6(b) to Fig. 6(d) show three possible results from our system's ExplicitProbView. In contrast to Fig. 6(a), it is clear that our three results could indicate the likelihoods of the green part being breast tumor. Also, the three results are revealed in a systematic method, by dragging the breast tumor's slider to query its probabilities. Compared to TF-based random adjustment, it is possible and quicker to use this systematic method to reveal all possible appearances of the breast tumor, which enables medical experts to make more comprehensive diagnosis or pre-operative planning. Moreover, as illustrated in Fig. 6(b) and Fig. 6(d), for each material such as the breast tumor, our system enables to reveal its two extreme cases, which could be used as boundary conditions to make a diagnosis and pre-operative planning decision.

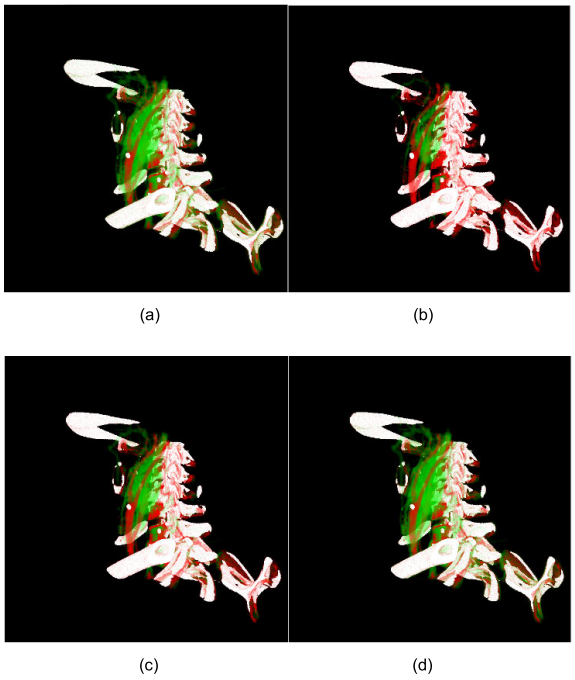

FIGURE 7. Renderings of CT Neck dataset in our system. Green represents thyroid tumor, red represents carotid arteries, and white represents bone. (a) shows the most possible appearance for thyroid tumor, carotid arteries and bone in the MaxProbView. (b)-(d) show thyroid tumor's three probability query results (from left to right, the thyroid tumor's probabilities are *99%*, *90%* and *50%*, respectively) in the ExplicitProbView.

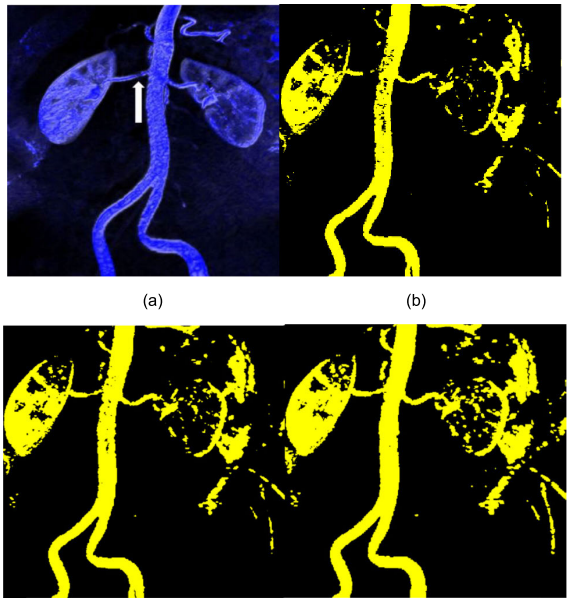

FIGURE 8. (a) shows a rendering of Renal Angiography dataset using traditional DVR (with shading enabled). (b)-(d) show vessel's three probability query results (from left to right, the vessel's probabilities are *50%*, *25%* and *5%*, respectively) in our system' ExplicitProbView.

The second example is to assess the extent of thyroid tumor in relation to carotid arteries. Medical experts could start the assessment by first inspecting the result from our system's MaxProbView, as illustrated in Fig. 7(a), which gives an

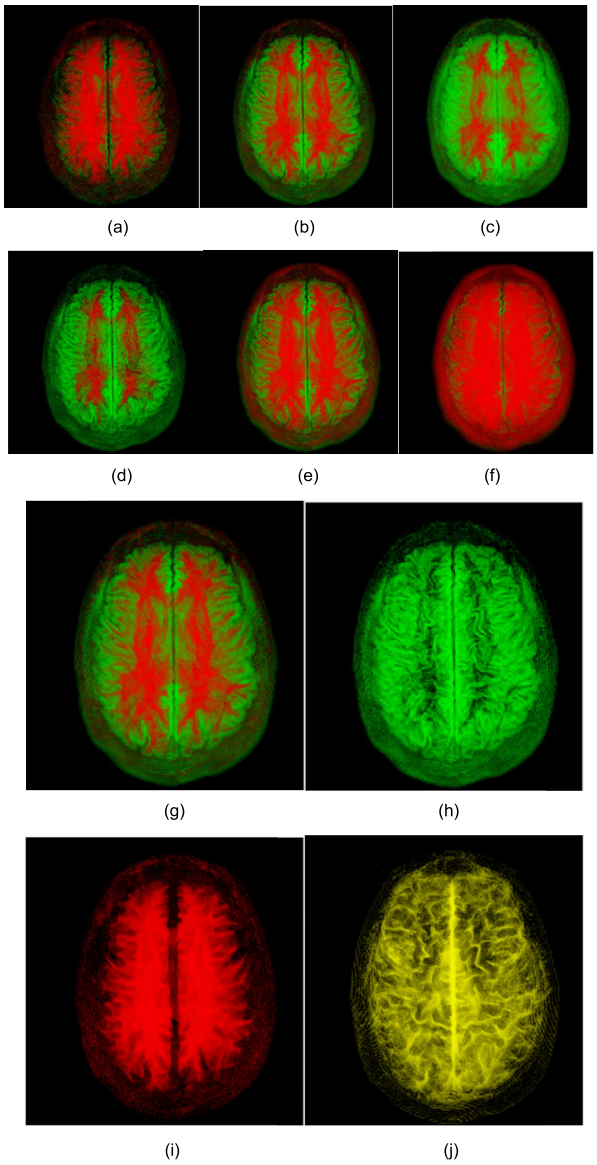

FIGURE 9. Renderings of Bruce dataset in our system. Green represents gray matter, red represents white matter, and yellow represents cerebrospinal fluid. (a)-(c) show gray matter's three probability query results (from left to right, gray matter's probabilities are *90%*, *50%* and *15%*, respectively) in relation to the most possible white matter in the ExplicitProbView. (d)-(f) show white matter's three probability query results (from left to right, white matter's probabilities are *99%*, *15%* and *1%*, respectively) in relation to the most possible gray matter in the ExplicitProbView. (g) shows the most possible appearance of both gray and white matters in the MaxProbView. (h)-(j) show the most possible appearance of a single material (from left to right: gray matter, white matter and cerebrospinal fluid) in the MaxProbView.

overview of the most possible appearance for all materials, and then drill down to the extent of thyroid tumor by dragging its slider for queries, and inspect the corresponding results in the ExplicitProbView, as illustrated in Fig. 7(b) to Fig. 7(d). Compared to traditional DVR, our system generates results that indicate quantitative extent of the thyroid tumor. It could also reveal all possible appearances as well as the two extreme cases of the thyroid tumor. Both cannot be done by using traditional DVR.

The third example is to determine if there is a vessel stenosis, as illustrated by the white arrow in Fig. 8(a), which is DVR of a Renal Angiography dataset. Using traditional DVR for such a task is risky, as it may not reveal the true result because of random adjustment of the TF, and thus makes medical experts determine that there is a stenosis. As a result, patient has to undergo an unnecessary operation. In comparison, our system enables medical experts to systematically explore the task, and thus could reveal all possible results in regard to the stenosis. Fig. 8(b) to Fig. 8(d) show the results from our system's ExplicitProbView, and it is clear from these results that there is no stenosis.

A final example is to distinguish gray matter and white matter of a human brain, which is a common clinical question. Using traditional DVR to explore such a task is time-consuming, and may be impossible to reveal a complete relationships between the gray matter and white matter. Also, it may be impossible to reveal the two extreme cases of the gray or white matter, which could be used as boundary conditions to make a diagnosis or pre-operative planning. In contrast, our system's ExplicitProbView enables medical experts quicker and easier to explore the relationships between gray matter and white matter from two perspectives: (1) exploring all possible appearances of the gray matter in relation to the most possible white matter, as illustrated in Fig. 9(a) to Fig. 9(c); (2) exploring all possible appearances of the white matter in relation to the most possible gray matter, as illustrated in Fig. 9(d) to Fig. 9(f). Moreover, for arbitrary one material such as white matter, our system enables to reveal its two extreme cases, as illustrated in Fig. 9(d) and Fig. 9(f), which could be used as boundary conditions for diagnosis or pre-operative planning decision. Fig. 9(g) shows the result from our system's MaxProbView, which indicates the most possible appearance of both gray matter and white matter. One thing deserves final mentioning is that compared to traditional DVR, our system enables more easily removing or adding materials for rendering, by simply setting transparency of each material. This feature is very useful for cases such as medical experts are interested in exploring the possible appearances of only one material, as illustrated in Fig. 9(h) and Fig. 9(j).

VI. CONCLUSION

This paper presented a probabilistic slider system, which can be used to visualize classification uncertainty in medical volume data. Compared to traditional DVR, it has the following advantages: (1) it generates results that could quantitatively indicate the probability of occurrence of arbitrary one material; (2) it enables to reveal all possible appearances of arbitrary one material in a quicker and systematic way; (3) it enables to reveal extreme cases of arbitrary one material, which can be considered as boundary conditions of a decision; (4) it enables more easily removing or adding materials for rendering; (5) it separates the classification task and optical property assignment task that are usually mixed in TF. As a result, it enables medical experts to make more accurate diagnosis or pre-operative planning decision, and have a clearer concept of how the medical volume data being classified.

From the color encoding methods mentioned in Section III.C one may notice that currently our system only enables users to form a single query for a material e.g., $p(M_A) \geq 90\%$ by dragging its slider, and do not enables to combine multiple slider values to form a compound query e.g., $p(M_A) \geq 90\%$ *AND* $p(M_B) \geq 80\%$. Our next step is to extend the current work to achieve compound query. As mentioned in [41], many types of uncertainty do exit in medical visualization, but not much research is focused on solving this problem. Therefore, another future work that we would like to conduct is to solve the uncertainties problems involved in medical visualization.

REFERENCES

[1] C. R. Johnson and A. R. Sanderson, "A next step: Visualizing errors and uncertainty," *IEEE Comput. Graph. Appl.*, vol. 23, no. 5, pp. 6–10, Sep. 2003.
[2] C. Johnson, "Top scientific visualization research problems," *IEEE Comput. Graph. Appl.*, vol. 24, no. 4, pp. 13–17, Jul. 2004.
[3] T. Munzner, C. Johnson, R. Moorhead, H. Pfister, P. Rheingans, and T. S. Yoo, "NIH-NSF visualization research challenges report summary," *IEEE Comput. Graph. Appl.*, vol. 26, no. 2, pp. 20–24, Mar./Apr. 2006, doi: 10.1109/MCG.2006.44.
[4] K. Brodlie, R. A. Osorio, and A. Lopes, "A review of uncertainty in data visualization," in *Expanding the Frontiers of Visual Analytics and Visualization*. London, U.K.: Springer, 2012, pp. 81–109, doi: 10.1007/978-1-4471-2804-5_6.
[5] K. Potter, P. Rosen, and C. R. Johnson, "From quantification to visualization: A taxonomy of uncertainty visualization approaches," in *Uncertainty Quantification in Scientific Computing*, vol. 377, A. Dienstfrey and R. Boisvert, Eds. Berlin, Germany: Springer, 2011, pp. 226–249.
[6] H. Lei, H. D. Chen, J. Y. Xu, X. Y. Wu, and W. Chen, "A survey on uncertainty visualization," *J. Comput.-Aided Des. Comput. Graph.*, vol. 25, no. 3, pp. 294–303, 2013.
[7] J. W. Tukey, *Exploratory Data Analysis*. Reading, MA, USA: Addison-Wesley, 1977.
[8] J. Sanyal, S. Zhang, G. Bhattacharya, P. Amburn, and R. Moorhead, "A user study to compare four uncertainty visualization methods for 1D and 2D datasets," *IEEE Trans. Vis. Comput. Graphics*, vol. 15, no. 6, pp. 1209–1218, Nov. 2009.
[9] K. Potter, J. Kniss, R. Riesenfeld, and C. R. Johnson, "Visualizing summary statistics and uncertainty," in *Computer Graphics Forum*, vol. 29, no. 3. Oxford, U.K.: Blackwell, 2010, pp. 823–831.
[10] C. M. Wittenbrink, A. T. Pang, and S. K. Lodha, "Glyphs for visualizing uncertainty in vector fields," *IEEE Trans. Vis. Comput. Graphics*, vol. 2, no. 3, pp. 266–279, Sep. 1996.
[11] A. T. Pang, C. M. Wittenbrink, and S. K. Lodha, "Approaches to uncertainty visualization," *Vis. Comput.*, vol. 13, no. 8, pp. 370–390, Nov. 1997.
[12] A. Pang, "Visualizing uncertainty in geo-spatial data," in *Proc. Workshop Intersections Geospatial Inf. Inf. Technol.*, 2001, p. 3823.
[13] T. S. Newman and W. Lee, "On visualizing uncertainty in volumetric data: Techniques and their evaluation," *J. Vis. Lang. Comput.*, vol. 15, no. 6, pp. 463–491, Dec. 2004.
[14] M. Hlawatsch, P. Leube, W. Nowak, and D. Weiskopf, "Flow radar glyphs—Static visualization of unsteady flow with uncertainty," *IEEE Trans. Vis. Comput. Graphics*, vol. 17, no. 12, pp. 1949–1958, Dec. 2011.
[15] F. Jiao, J. M. Phillips, Y. Gur, and C. R. Johnson, "Uncertainty visualization in HARDI based on ensembles of ODFs," in *Proc. IEEE Pacific Vis. Symp.*, Feb. 2012, pp. 193–200.
[16] G. Grigoryan and P. Rheingans, "Point-based probabilistic surfaces to show surface uncertainty," *IEEE Trans. Vis. Comput. Graphics*, vol. 10, no. 5, pp. 564–573, Sep. 2004.
[17] P. J. Rhodes, R. S. Laramee, R. D. Bergeron, and T. M. Sparr, "Uncertainty visualization methods in isosurface rendering," in *Eurographics*. Girona, Spain: Eurographics Association, 2003, pp. 83–88.

[18] M. Paul, N. J. Mitra, and L. Guibas, "Uncertainty and variability in point cloud surface data," in *Proc. Eurograph. Symp. Point-Based Graph.* London, U.K.: Eurographics Association Press, 2004, pp. 77–84.
[19] R. A. Osorio and K. Brodlie, "Contouring with uncertainty," in *Theory and Practice of Computer Graphics*. London, U.K.: Eurographics Association, 2008, pp. 59–66.
[20] R. A. Osorio and K. Brodlie, "Uncertain flow visualization using LIC," in *Theory and Practice of Computer Graphics*. London, U.K.: Eurographics Association, 2009, pp. 1–9.
[21] A. Foulks and R. D. Bergeron, "Uncertainty visualization in the VisIt visualization environment," in *Visualization and Data Analysis*. Bellingham, WA, USA: SPIE, 2009, pp. 72430–72440.
[22] S. Djurcilov, K. Kim, P. Lermusiaux, and A. Pang, "Visualizing scalar volumetric data with uncertainty," *Comput. Graph.*, vol. 26, no. 2, pp. 239–248, Apr. 2002.
[23] V. Dinesha, N. Adabala, and V. Natarajan, "Uncertainty visualization using HDR volume rendering," *Vis. Comput.*, vol. 28, no. 3, pp. 265–278, Mar. 2012.
[24] T. Strothotte, M. Puhle, and M. B. Masuch, "Visualizing uncertainty in virtual reconstructions," *Proc. EVA Eur., Comput. Soc.*, 1999, pp. 1–16.
[25] C. H. Lee and A. Varshney, "Representing thermal vibrations and uncertainty in molecular surfaces," in *Proc. SPIE Conf. Vis. Data Anal., Int. Soc. Opt. Photon.*, Mar. 2002, pp. 80–90.
[26] A. Coninx, G.-P. Bonneau, J. Droulez, and G. Thibault, "Visualization of uncertain scalar data fields using color scales and perceptually adapted noise," in *Proc. ACM SIGGRAPH Symp. Appl. Perception Graph. Vis. (APGV)*, 2011, pp. 59–66.
[27] V. Interrante, "Harnessing natural textures for multivariate visualization," *IEEE Comput. Graph. Appl.*, vol. 20, no. 6, pp. 6–11, Nov. 2000.
[28] R. P. Botchen, D. Weiskopf, and T. Ertl, "Texture-based visualization of uncertainty in flow fields," in *Proc. VIS IEEE Vis.* Los Alamitos, CA, USA: IEEE Computer Society Press, 2005, pp. 654–657.
[29] R. P. Botchen, D. Weiskopf, and T. Ertl, "Interactive visualization of uncertainty in flow field using texture-based techniques," in *Proc. 12th Int. Symp. Flow Vis.* Los Alamitos, CA, USA: IEEE Computer Society Press, 2006, pp. 4051–4056.
[30] K. Potter, A. Wilson, P.-T. Bremer, D. Williams, C. Doutriaux, V. Pas, and C. R. Johnson, "Ensemble-vis: A framework for the statistical visualization of ensemble data," in *Proc. IEEE Int. Conf. Data Mining Workshops*, Dec. 2009, pp. 233–240.
[31] B. Zehner, N. Watanabe, and O. Kolditz, "Visualization of gridded scalar data with uncertainty in geosciences," *Comput. Geosci.*, vol. 36, no. 10, pp. 1268–1275, Oct. 2010.
[32] A. Cedilnik and P. Rheingans, "Procedural annotation of uncertain information," in *Proc. IEEE Vis.*, Oct. 2000, pp. 77–84.
[33] J. Sanyal, S. Zhang, J. Dyer, A. Mercer, P. Amburn, and R. J. Moorhead, "Noodles: A tool for visualization of numerical weather model ensemble uncertainty," *IEEE Trans. Vis. Comput. Graphics*, vol. 16, no. 6, pp. 1421–1430, Nov. 2010.
[34] G. S. Schmidt, S.-L. Chen, A. N. Bryden, M. A. Livingston, L. J. Rosenblum, and B. R. Osborn, "Multidimensional visual representations for underwater environmental uncertainty," *IEEE Comput. Graph. Appl.*, vol. 24, no. 5, pp. 56–65, Sep. 2004.
[35] T. Pfaffelmoser, M. Reitinger, and R. Westermann, "Visualizing the positional and geometrical variability of isosurfaces in uncertain scalar fields," *Comput. Graph. Forum*, vol. 30, no. 3, pp. 951–960, Jun. 2011.
[36] K. Pothkow and H.-C. Hege, "Positional uncertainty of isocontours: Condition analysis and probabilistic measures," *IEEE Trans. Vis. Comput. Graphics*, vol. 17, no. 10, pp. 1393–1406, Oct. 2011.
[37] K. Pothkow, B. Weber, and H. C. Hege, "Probabilistic marching cubes," *Comput. Graph. Forum*, vol. 30, no. 3, pp. 931–941, 2011.
[38] R. Brown, "Animated visual vibrations as an uncertainty visualisation technique," in *Proc. 2nd Int. Conf. Comput. Graph. Interact. Techn. Austalasia Southe East Asia (GRAPHITE)*, 2004, pp. 84–89.
[39] C. Lundstrom, P. Ljung, A. Persson, and A. Ynnerman, "Uncertainty visualization in medical volume rendering using probabilistic animation," *IEEE Trans. Vis. Comput. Graph.*, vol. 13, no. 6, pp. 1648–1655, Nov. 2007.
[40] C. Lundstrom, "Efficient medical volume visualization: An approach based on domain knowledge," Dept. Sci. Technol., Linkoping Univ., Linköping, Sweden, 2007.
[41] G. Ristovski, T. Preusser, H. K. Hahn, and L. Linsen, "Uncertainty in medical visualization: Towards a taxonomy," *Comput. Graph.*, vol. 39, pp. 60–73, Apr. 2014.
[42] B. Wolfgang, *Applied Medical Image Processing: A Basic Course*, 2nd ed. Boca Raton, FL, USA: CRC Press, 2014.
[43] K.-S. Chuang, H.-L. Tzeng, S. Chen, J. Wu, and T.-J. Chen, "Fuzzy C-means clustering with spatial information for image segmentation," *Comput. Med. Imag. Graph.*, vol. 30, no. 1, pp. 9–15, Jan. 2006.

JI MA received the master's and Ph.D. degrees from University College Cork (UCC), Ireland. He is currently a Lecturer with the School of Computer Science and Technology, Zhejiang University of Technology. His major research interest includes data visualization.

JINJIN CHEN received the bachelor's and master's degrees from Jiangnan University. She is currently a Lecturer with the School of Design and Art, Communication University of Zhejiang. Her major research interests include virtual reality and interactive design.

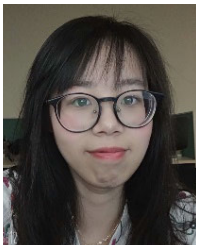

LIYE CHEN is currently a Radiologist with the Sir Run Run Shaw Hospital, School of Medicine, Zhejiang University.

JIAZHOU CHEN received the dual Ph.D. degrees from the INRIA Bordeaux Sud-Ouest, France, and the State Key Laboratory of CAD and CG, Zhejiang University, China, in 2012. He is currently an Associate Professor with the School of Computer Science and Technology, Zhejiang University of Technology. His research interests include computer graphics and visual media computing.

XUJIA QIN is currently a Professor with the School of Computer Science and Technology, Zhejiang University of Technology. His research interests include data visualization, computer graphics, digital image processing, and geometric modeling.

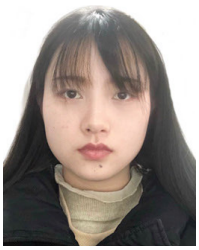

MINGYU BAO is currently pursuing the master's degree with the School of Computer Science and Technology, Zhejiang University of Technology. Her major research interest includes scientific visualization.